

www.acsnano.org

Dipeptide Nanostructure Assembly and Dynamics via in Situ Liquid-Phase Electron Microscopy

Karthikeyan Gnanasekaran,[#] Joanna Korpanty,[#] Or Berger, Nicholas Hampu, Michal Halperin-Sternfeld, Dana Cohen-Gerassi, Lihi Adler-Abramovich, and Nathan C. Gianneschi*



Cite This: ACS Nano 2021, 15, 16542–16551



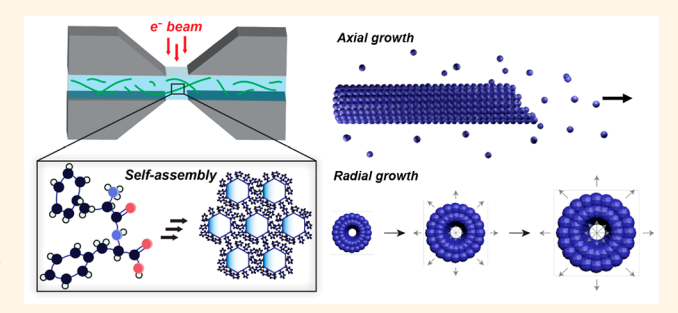
ACCESS

Metrics & More

Article Recommendations

Supporting Information

ABSTRACT: In this paper, we report the *in situ* growth of FF nanotubes examined *via* liquid-cell transmission electron microscopy (LCTEM). This direct, high spatial, and temporal resolution imaging approach allowed us to observe the growth of peptide-based nanofibrillar structures through directional elongation. Furthermore, the radial growth profile of FF nanotubes through the addition of monomers perpendicular to the tube axis has been observed in real-time with sufficient resolution to directly observe the increase in diameter. Our study demonstrates that the kinetics, dynamics, structure formation, and assembly mechanism of these supramolecular



assemblies can be directly monitored using LCTEM. The performance of the peptides and the assemblies they form can be verified and evaluated using *post-mortem* techniques including time-of-flight secondary ion mass spectrometry (ToF-SIMS).

KEYWORDS: dipeptides, diphenylalanine, self-assembly, liquid-cell TEM, ToF-SIMS

INTRODUCTION

Diphenylalanine (FF) nanotubes have attracted attention for their relation to amyloid fibers that are associated with the development of neurological diseases including Alzheimer's disease and type II diabetes. 1-4 The biological importance of FF has inspired numerous research efforts, ranging from directed self-assembly to functional biomaterials with mechanical, thermal, piezoelectric, luminescence, semiconductive, and waveguide properties. 5-10 FF nanotubes spontaneously form by first solubilizing diphenylalanine in water at 80 °C, followed by cooling to room temperature. 11 To date, the majority of studies on the kinetics, dynamics, dimensions, and phase transitions of FF supramolecular assemblies have been performed by conventional bulk solution characterization techniques, which largely reveal ensemble behavior and lack direct insight into the dynamics and morphology of individual nanotubes. 12,13 The ability to visualize the assembly, dynamics, and formation of FF in real-time with nanometer resolution would enable the elucidation of the assembly pathways and phase transformations. Moreover, a deeper understanding of FF dynamics would build a methodological basis for the future visualization of cellular machinery like actin filaments, tubulin (de)polymerization events, and pathophysiological processes such as amyloid fibril formation.

To probe the solution-phase dynamics of FF, liquid-cell transmission electron microscopy (LCTEM), an in situ imaging technique that enables high resolution insight into solvated nanomaterials, can be employed. The typical LCTEM platform hermetically seals a liquid sample between two silicon microchips that are fabricated with an electron transparent silicon nitride viewing window (Figure S1). 14,15 Moreover, variable temperature (VT) LCTEM enables in situ heating of solvated nanomaterials, allowing one to probe temperaturetriggered dynamics.¹⁶ Recent developments in LCTEM have shown its potential in imaging solvated materials, dynamics, and structure formation with high spatial and temporal resolution. LCTEM has been widely applied to study the nucleation, growth, and dynamics of inorganic nanomaterials. $^{17-21}$ However, there are limited studies on soft materials, $^{22-24}$ hybrid materials, $^{25-27}$ and biomaterials, $^{28-30}$ as these materials are inherently limited by low contrast and by

Received: July 20, 2021 Accepted: September 30, 2021 Published: October 8, 2021





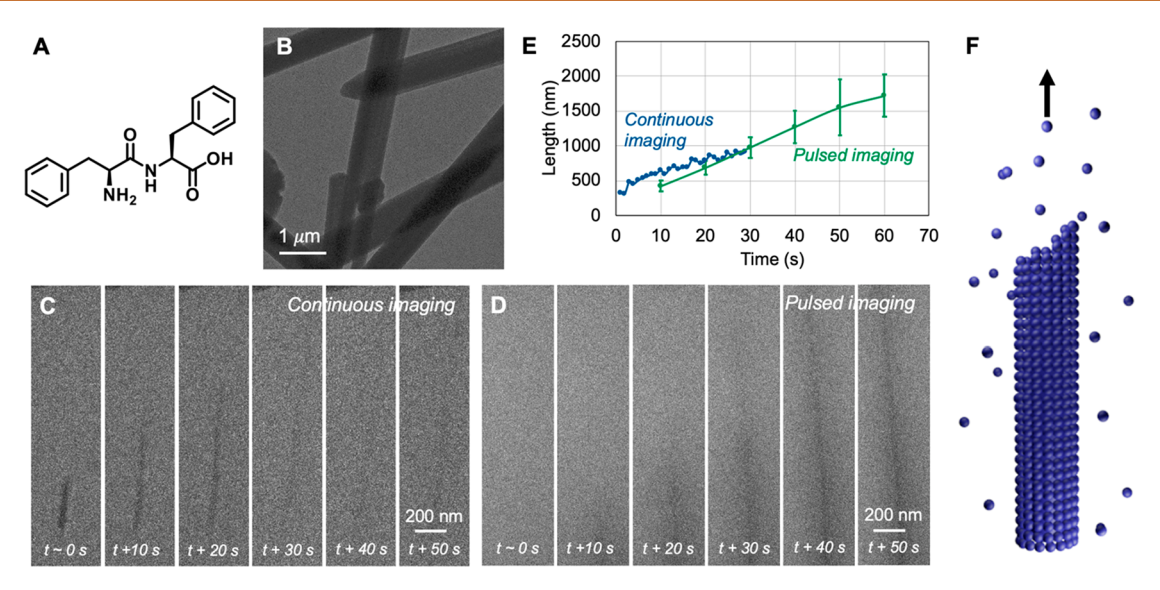


Figure 1. LCTEM of FF self-assembly. FF monomers were added to deionized water, placed in the liquid-cell, heated at 80 °C for 1 h and allowed to cool to room temperature for 30 min. (A) Chemical structure of FF monomer. (B) Dry state TEM of FF assemblies. (C) Time lapsed LCTEM snapshots of FF nanotube growth acquired with an instantaneous flux of 0.3 e⁻ Å⁻² s⁻¹ (continuous imaging). Structural damage is observed as the cumulative fluence reaches 9 e⁻ Å⁻². (D) LCTEM snapshots of FF nanotube growth captured by a time lapse of 10 s interval with a flux of 0.5 e⁻ Å⁻² s⁻¹ (pulsed imaging). (E) Length of FF nanotube as a function of time illustrates the linearity in the elongation of FF nanotubes captured by continuous imaging and pulsed imaging. The error bars represent the average and 1 σ of three independent measurements. (F) Schematic illustration of FF monomers association and dissociation events leading to the growth of nanotubes.

their electron beam sensitivity. Indeed, success in LCTEM experiments heavily depends on the flux (e- Å-2 s-1) and fluence $(e^- \ \mathring{A}^{-2})$ used to observe a given nanoscale process. ^{31–33} Solvated soft materials typically experience radiation damage by undergoing secondary reactions with radicals produced from solvent radiolysis, causing a perturbation in the chemistry and dynamics of the nanomaterials under investigation. 34–38 The analysis of the liquid-cell chips after imaging (i.e., post-mortem analysis) can be performed to verify morphology and the extent of the electron beam effects in the observed dynamic process. 25,26,39 Specifically for polymers and peptides, we have reported the use of matrix-assisted laser desorption/ionization imaging mass spectrometry (MALDI-IMS) to characterize the extent of electron beam damage at the chemical level. 35,40 Here, we observe FF assemblies in real-time via LCTEM and examine the effect of the electron beam through post-mortem surface characterization via time-of-flight secondary ion mass spectroscopy (ToF-SIMS).

RESULTS AND DISCUSSION

For the formation of FF assemblies within the TEM liquid-cell (for schematic showing the cell setup see, Figure S1), first, 2 mg mL $^{-1}$ FF in deionized water was placed inside the cell, where it was heated to 80 °C for 1 h and allowed to cool to room temperature for 30 min (Figure 1). The FF peptide assembles into elongated discrete nanostructures, as visualized by dry state TEM (Figure 1A,B). Nanotube formation from FF peptides could be directly and continuously videoed with a flux of 0.3 e $^{-}$ Å $^{-2}$ s $^{-1}$ (Figure 1C, Figure S2A, and Movie S1). However, with continuous irradiation, the nanotube growth was eventually impeded, and the assemblies began to redissolve, demonstrating visible structural damage to the assemblies at a fluence (cumulative dose) of \sim 9 e $^{-}$ Å $^{-2}$. With fluence constraints established, the growth of FF nanotubes could then be examined by applying a pulsed imaging

method.⁴¹ To achieve this, we employed a flux of 0.5 e⁻ Å⁻² s⁻¹ for a duration of 1 s at a time, with the beam blanked for 10 s at a time between 1 s acquisitions. Subsequent repeat acquisitions revealed FF nanotube assembly with a cumulative fluence of 3 $e^- Å^{-2}$ (Figure 1D, Figure S2B). The growth rate, measured via continuous imaging or via pulsed imaging, varied only by a factor of ~1.5, which demonstrates the viability of pulsed imaging protocols for dynamic imaging for an extended period with minimum fluence (Figure 1E). This direct videography performed with high spatial and temporal resolution reveals the growth of individual peptide fibrils. The growth of individual fibrils from monomers proceeds by addition to the end of the fibrils at a rate of $\sim 20 - \sim 25$ nm s⁻¹. The unidirectional elongation and growth rate observed by in situ LCTEM are in good agreement with growth measurements obtained using microfluidics devices, which have micrometer spatial resolution. 42,43 Mechanistically, there is a thermodynamic driving force for monomers to associate by intermolecular interactions, specifically interpeptide hydrogen bonding of main chains and $\pi - \pi$ stacking between the hydrogen bonded main chains. 1,2 This leads to the formation of hydrophilic channels with a van der Waals diameter of 1 nm surrounded by hydrophobic aromatic side chain residues of the FF monomers. Growth occurs via elongation and dissociation events, with a net growth rate linear with respect to the local monomer concentration. 42 The initially formed assembly tends to preferentially attract free monomers along the nanotube long axis, where the majority of the oxygen atoms are positioned asymmetrically, resulting in unidirectional elongation (Figure 1F).42

To the best of our knowledge, the radial growth profile of FF nanotubes through the addition of monomers perpendicular to the tube axis has never been observed. That is, it has not been possible to image individual nanotubes growing in real-time with sufficient resolution to see them increase in diameter.

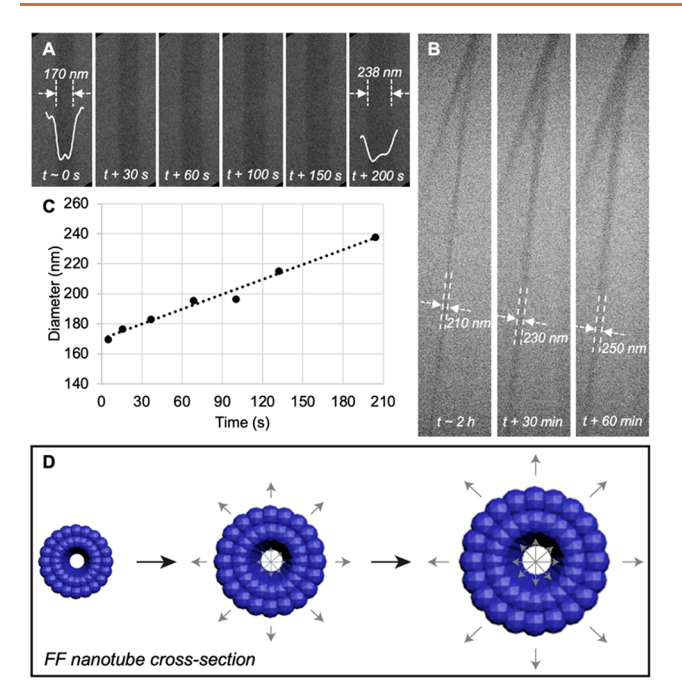


Figure 2. Radial growth of FF nanotubes by LCTEM. FF monomers were added to deionized water, placed in the liquid-cell, heated at 80 °C for 1 h, and allowed to cool to room temperature for 30 min. (A and B) LCTEM snapshots of radial growth of FF nanotube with integrated line profiles illustrating the increase in tube diameter and hollowness of the nanotube. Data acquired with an instantaneous flux of 0.3 e $^{-}$ Å $^{-2}$ s $^{-1}$. (C) Outer diameter plotted as a function of time shows the linear trend in increase in diameter. (D) Schematic of FF nanotube cross-section illustrates the association and dissociation events leading to the increase in tube diameter with time.

Here, the nanometer spatial resolution of LCTEM revealed the radial growth of FF nanostructures (Figure 2). The line profile across the nanotube illustrates the hollowness of the structure, which confirms that FF monomers indeed self-assemble into nanotubes (Figure 2A, Figure S3A). While in bulk solution, nanotubes can grow to millimeters axially and hundreds of microns radially (Figure 1B, Figure S3B), confinement within the liquid-cell eventually limits both radial and axial growth of the nanotubes, with little change in dimension after 3 h following initiation of the reaction (Figure 2B). Precise measurement at various time points further showed a linear growth trend in inner and outer diameters, with an aspect ratio proportional to the square root of time (Figure 2C, Figure S4). These results indicate that, in addition to monomer addition leading to axial nanotube growth, the association and dissociation of FF monomers occurs radially, resulting in changes to both the diameter of the hollow core and the wall thickness (Figure 2D). By prying open the liquid-cell assembly after growth experiments, we could then subsequently image in the dry state, where we observed long nanotubes formed elsewhere within the liquid-cell outside the field of view, proving that the observed growth is not dependent on or driven by the electron beam (Figure S5).

Prior reports have shown that FF monomers form irregular disordered oligomers that transform into double layered assemblies that subsequently close to form vesicles and the fusion of vesicles to ring-like motifs that undergo further elongation to form nanotubes. To observe these intermolecular interactions, we imaged the assemblies during

the nucleation process, that is, immediately after cooling from 80 °C. Due to low flux limitations, our imaging conditions produced only limited contrast and resolution, restricting our ability to capture intermolecular dynamics. Nevertheless, we observed the appearance of hollow nanostructures resembling the ring-like FF motifs that spontaneously organized in less than ~3 min of cooling (Figure 3, Movie S2). Time lapse snapshots revealed the immediate formation of oligomers and their aggregation to ring-like motifs (Figure 3A-C). At first, hydrophobic side chains of FF molecules reduced their exposure to water by stacking and exposing their backbones to water molecules. This spontaneous intermolecular interaction results in parallel β -sheet-like structures, with a majority of side chains on one side, which creates a favorable interface for further stacking to form oligomers of a few nanometers as observed by LCTEM. The aggregation of these oligomers by further hydrophobic stacking and electrostatic interactions at the termini to further reduce the entropy of the system results in larger supramolecular ring-like motifs (arrows in Figure 3C,D, Figure S6).⁴⁷ This structural motif formation event was captured by LCTEM. However, the elongation of these structures was not observed by continuing the reaction within the liquid-cell. The inability to visualize the subsequent elongation to nanofibrils is likely due to concentration constraints. The multistep assembly pathway of FF molecules follows a complex free energy landscape with diverse molecular geometries of comparable free energies such that the ultimate assembly pathway is finely controlled by the conformation fluctuations and local monomer concentration. 45 To verify the effect of local monomer availability within the liquid-cell, we performed a series of off-line (outside the electron microscope) LCTEM experiments over a prolonged period. Here, we observed that, while maintaining the liquid-cell under static conditions, all the monomers were assembled into long micron sized, anisotropic nanotubes, whereas a continuous flow of water led to smaller, isotropic spherical assemblies (Figure S7). This inconsistency in the morphology represents the delicate monomer and water interactions, where a constant flow of water into the liquid-cell depletes free monomers and dissociates FF molecules from the nanotube, resembling assembly behavior under subcritical concentrations. 42 It should be noted that these phenomena could be distinctive to LCTEM, as the reaction takes place under confined conditions and is heavily affected by the liquid thickness, ⁴⁸ heterogeneity in local concentration, ⁴⁹ silicon nitride surface chemistry, ⁵⁰ and water/air interfacial effects. ⁵¹ For example, we also observed that preformed FF nanotubes with identical concentration remain intact within the liquid-cell and do not dissociate into constituent monomers upon heating, further supporting the effect of imbalance in water and dipeptide concentration within the liquid-cell (Figure S8). Hence, it is likely that optimum FF nanotubes growth conditions may not be achieved at every instance and specifically in the imaged area. To complement these growth measurements by LCTEM, ensemble-averaged FF assembly in bulk conditions was studied using in situ scattering techniques (Figure S9). The scattering analyses suggest that FF molecules self-assemble to form nanostructures larger than ~250 nm rapidly upon cooling from 80 °C, making scattering methods nonviable for tracking the early stage growth of FF in bulk conditions. Further combined, these observations indicate that nucleation and growth kinetics were slower within the liquid-cell compared to the bulk, mainly

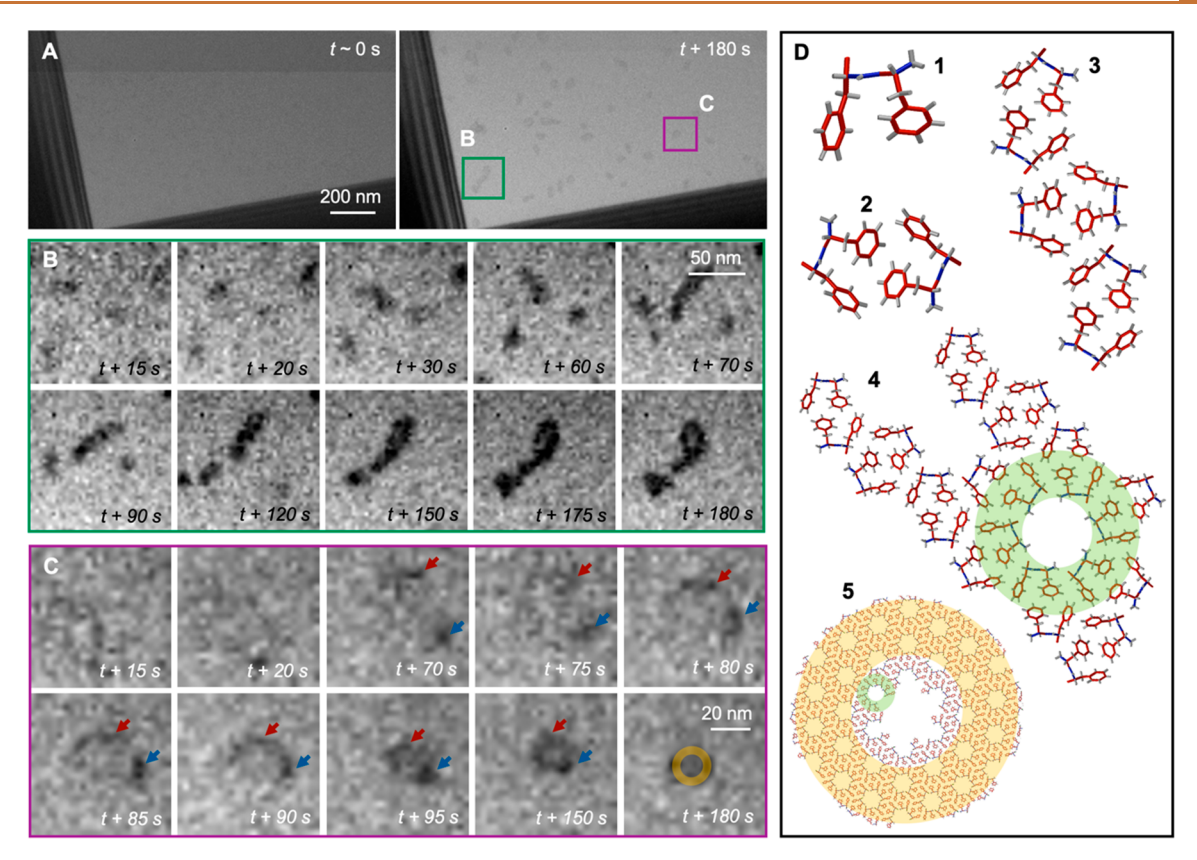


Figure 3. LCTEM of early stage assemblies of FF molecules. FF monomers were added to deionized water, placed in the liquid-cell, heated at 80 °C for 1 h, and allowed to cool to room temperature. (A) LCTEM overview snapshots after the initiation of cooling cycle. Data acquired with an instantaneous flux of $0.3~{\rm e^-}~{\rm Å^{-2}~s^{-1}}$. (B and C) Time-lapse LCTEM of FF oligomers and aggregation to form ring-like motifs. (D) Schematic illustration of FF assembly due to hydrophobic interaction of monomers to form oligomers and ring-like motifs.

controlled by mass transport limitations in the confined environment.

Critical to the success of LCTEM experiments and to our ability to interpret LCTEM data is our understanding of how radiolytic beam damage perturbs the system. Radiolytic chemical processes, such as oriented attachment,⁵² nanoparticle aggregation,⁵³ and shape-directed⁵⁴ assembly mechanisms, are commonly reported in LCTEM experiments. In general, under ionizing radiation, water molecules undergo radiolysis to form reactive radicals and molecular species. Of particular importance are the strongly reducing aqueous electron (e-an) and hydrogen radical (•H) and the strongly oxidizing hydroxyl radical (*OH). *H and *OH react rapidly with organic molecules, leading to hydrogen abstraction and radical formation. Among the radicals produced from water radiolysis, OH radicals are considered to play a significant role in radiolytic damage. 34-36 In FF, OH radicals could rapidly react with the aromatic ring, amine, saturated alkanes, amide, and carbonyl groups; *H radicals react similarly but are less reactive; and e areacts rapidly with the carbonyl groups. 55-58

To gauge the influence of the electron beam on FF assemblies, we performed electron beam damage experiments under two conditions; in one experiment, the liquid-cell was imaged at low flux (\sim 0.5 e⁻ Å⁻² s⁻¹) and, in the other, at high flux (\sim 100 e⁻ Å⁻² s⁻¹) for 15 min at each of the four corners of the liquid-cell (Figure 4, Figure S10A–E, and Movies S3 and S4). Thus, each imaging event involved fluences of 4.5 \times 10² and 9 \times 10⁴ e⁻ Å⁻², and the cumulative fluences of the entire liquid cell were 18 \times 10² and 36 \times 10⁴ e⁻ Å⁻² for low flux and high flux conditions, respectively. During the experiment, the

assemblies remained intact under low electron flux and aggregated to form anisotropic chains under high electron flux. The quantitative analysis of LCTEM video frames showed a constant number of assemblies while imaging at 0.5 e⁻ Å⁻² s^{-1} until a fluence of 4.5 \times 10² e⁻ Å⁻² (Figure S10C). In contrast, the use of a higher electron flux led to a drastic increase followed by a gradual decline in the number of assemblies (Figure S10C). These data show that the assemblies are drawn to the imaged area while a higher flux is applied and aggregates when the fluence reaches $4.5 \times 10^4 \, \mathrm{e}^{-1}$ $Å^{-2}$. The accumulation of assemblies in the imaged area can also be quantified by measuring the increase in area over time (Figure S10D). The degree of aggregation was quantified by eccentricity, e, where an ellipse with e = 0 represents a circle, e= 1 represents a line segment, and 0 < e < 1 represents an ellipse with increasing aspect ratio (Figure S10E). The eccentricity of assemblies under low flux was almost constant at e = 0.7, which indicates that preformed individual assemblies were slightly oblong. The gradual increase in eccentricity under high flux conditions agrees with the observed accumulation and aggregation of assemblies. Though we cannot be certain about the underlying radiolytic reaction, we believe that the displacement of water molecules under the electron beam "steers" the small assemblies of FF and draws the assemblies closer to each other. This creates a favorable condition for the aromatic side chain π – π stacking of the individual assemblies to form elongated "necklace"-like morphologies. It has been shown that cationic dipeptides exhibit reversible tube-tovesicle-like morphologies with a similar necklace-like inter-

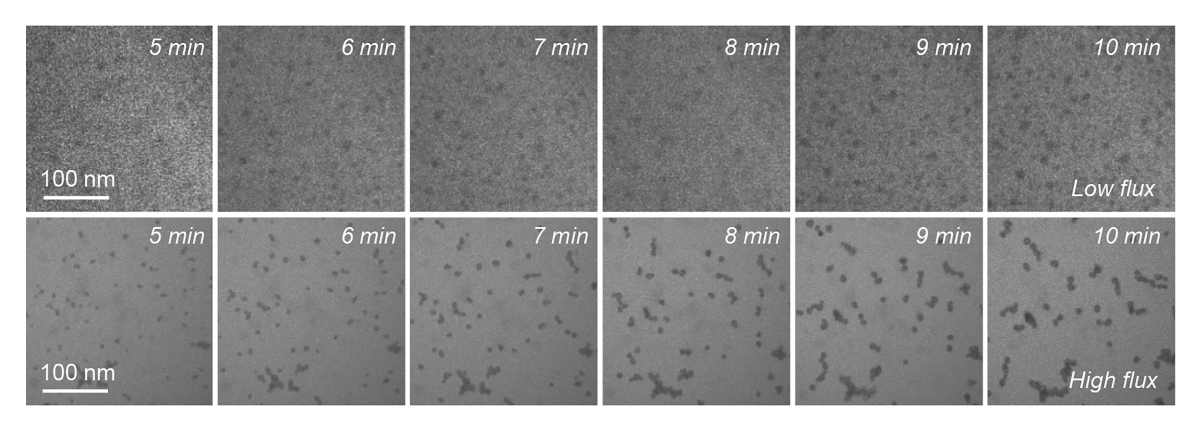


Figure 4. LCTEM of preformed FF assemblies in water at various flux conditions. Time lapsed LCTEM snapshots at a low flux (\sim 0.5 e⁻ Å⁻² s⁻¹) and a high flux (\sim 100 e⁻ Å⁻² s⁻¹).

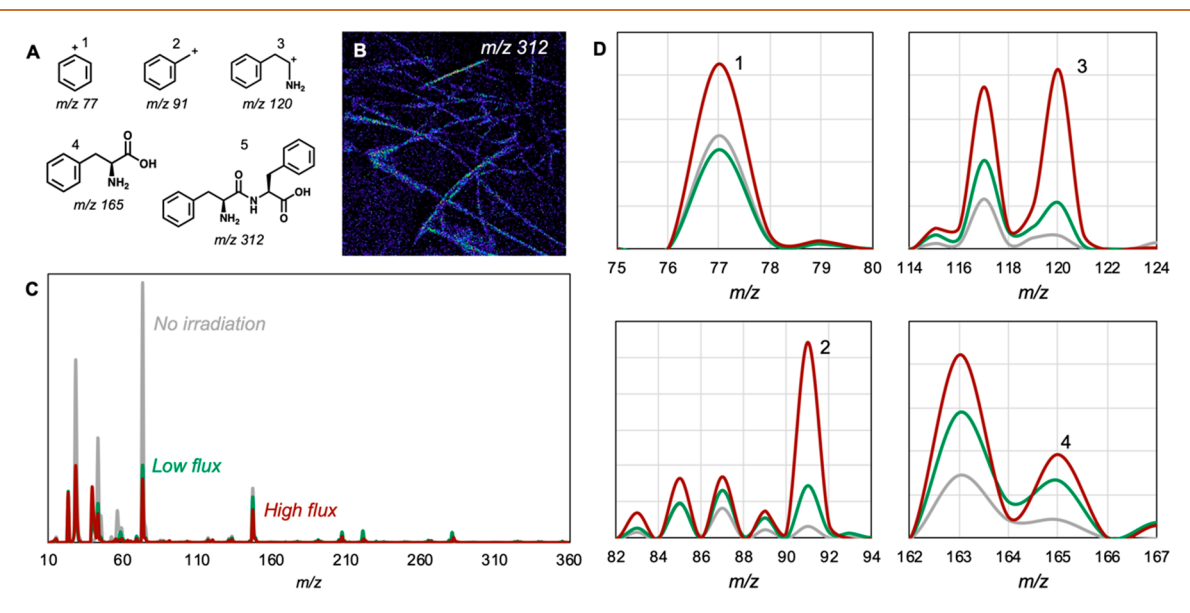


Figure 5. ToF-SIMS post-mortem analysis of FF assemblies within the liquid-cell. FF assemblies were irradiated with a flux of $0.5 \text{ e}^-\text{ Å}^{-2} \text{ s}^{-1}$ (low flux) and $100 \text{ e}^-\text{ Å}^{-2} \text{ s}^{-1}$ (high flux). (A) Chemical structures of potential fragments of FF generated by the electron beam. (B) Mass-filtered image of characteristic peaks of FF at m/z 312 \pm 1. (C) Normalized ToF-SIMS spectra of FF nanotubes subjected to electron irradiation under various flux. (D) ToF-SIMS spectra normalized by m/z 312 illustrating the relative change in the intensity of FF fragments at m/z 77, 91, 120, and 165 under various flux conditions.

mediate morphology with changes in dipeptide concentration. 12

Given the possibility of destruction of the FF molecules by reactive radical species even under low electron flux conditions, we subjected the imaged liquid-cell chips to post-mortem analysis via time-of-flight secondary ion mass spectroscopy (ToF-SIMS) (Figure 5). ToF-SIMS is a mass spectral technique in which a high energy ion beam bombards a surface, resulting in the emission of ions characteristic of the sample.⁵⁹ ToF-SIMS allows for high spatial and mass resolution mapping of analytes on a surface and is especially suited for studying low molecular weight (<500 Da) analytes. Mosaic mapping on a 0.5 mm \times 0.5 mm area surrounding the irradiated window was performed on each irradiated liquid-cell chip to yield a secondary ion map of the SiN_x surface. The m/zpeaks of interest corresponding to FF and its fragments are m/z 77, 91, 120, 165, and 312 (Figure 5A). 60 Mass-filtered secondary ion maps at m/z 312 \pm 1 further reveal the location and morphology of FF nanotubes (Figure 5B, Figure S11).60 Notably, the signal intensity of FF molecules shows a change in the intensity of peaks within the fragmentation pattern even

under low flux conditions (Figure 5C, Figure S12). The mass difference on the irradiated liquid-cell chips is also evident on the secondary ion maps, such that the distinct morphology of FF nanotubes is not visible at m/z 312 \pm 1, suggesting molecular level damage across the nanotubes even under low flux conditions (Figures S13 and S14). It should be noted that the lack of a signal at m/z 312 \pm 1 could also be due to the smearing of sample during prying apart of the liquid-cell assembly. Hence, we analyzed the intensity of FF fragments relative to the intensity of the FF molecule by normalizing the spectra with respect to m/z 312. This normalization procedure shows the increase in signal intensity at m/z 77, 91, 120, and 165 with increased electron flux, suggesting that the beam drives the breakdown of diphenylalanine to its constituent fragments (Figure 5D). Notably, the increase in signal at m/z 165 ± 1 indicates that the fragmentation of FF to phenylalanine can be initiated by the electron beam. However, though degradation is seemingly unavoidable, less fragmentation of FF to its constituent fragments was observed under low flux conditions compared to high flux conditions as we expect, correlated with our ability to acquire images of the fibrils at low

flux. In addition, to elucidate the mechanism of aggregation of preformed assemblies under high electron flux (Figure 4), we analyzed the m/z peaks beyond 400 (Figure S15—from m/z 400 to 800). Though the presence of an additional peak at m/z 510 \pm 1 could indicate interlocking of fragmented dipeptides to form necklace-like assemblies, most of the peaks disappeared compared to nonirradiated FF.

Recently, we have shown that the addition of *OH radical scavengers, such as alcohols, can mitigate indirect damage to soft materials during LCTEM analysis.35 On the basis of this observation, we performed LCTEM beam damage experiments on 0.2 µL of preformed 2 mg mL⁻¹ FF dipeptides dispersed in ethanol and isopropyl alcohol (IPA). We then imaged the liquid-cell at low flux ($\sim 0.5 \text{ e}^{-} \text{ Å}^{-2} \text{ s}^{-1}$) conditions for 15 min and with an extremely low fluence of $\sim 1 \text{ e}^-\text{ Å}^{-2}$ (0.1 e⁻ Å⁻² s⁻¹). Micrometer long FF nanotubes were observed in the liquid-cell and remained intact with no visible damage as the fluence reached $4.5 \times 10^2 \text{ e}^- \text{ Å}^{-2}$ (Figures S16–S21). The intactness of the preformed nanotubes implies they are more stable compared to the self-assembling nanotubes under the electron beam (Figure 1C). This suggests that the structural disintegration of self-assembling nanotubes by irradiation is primarily due to direct damage to the noncovalent interaction sites, such as the π - π stacking of side chains and hydrogen bonding motifs -NH₃+···-OOC- formed during the assembly process.1 Notably, under the same imaging and defocus conditions, the edge sharpness (resolution) of FF nanotubes observed in situ was improved in the order of IPA to ethanol to water (Figure S22). This clear trend in resolution of FF nanotubes in situ is primarily due to the lessening of scattering effects and beam broadening as the mean free path of electrons decreases from IPA to ethanol to water.⁶¹ These results point to the possibility of using less dense solvents to improve resolution in situ. The post-mortem ToF-SIMS analysis of FF nanotubes dispersed in alcohols showed a similar molecular level damage as observed in FF nanotubes dispersed in water (Figures S23-S30). These results further support that molecular level damage was primarily due to the direct damage to the FF nanostructures rather than indirect radiolytic reactions such as solvent radiolysis. 62 More importantly, these analyses demonstrate that characteristic m/z peaks of dipeptides or other low molecular weight organic materials can be analyzed by ToF-SIMS following LCTEM experiments to measure the survival of the material under electron beam irradiation.

CONCLUSION

In summary, we have shown the growth and dynamics of diphenylalanine assemblies with nanometer resolution via LCTEM. We note that the strict electron dose damage threshold of FF molecules limits the use of persistent electron beam exposure to capture growth over prolonged time scales. We have shown this can be circumvented by the application of pulsed imaging protocols with minimum fluence. The critical electron dose threshold of preformed FF assemblies is higher than the dose threshold of self-assembling FF. This indicates that FF assemblies undergo direct damage at the noncovalent interaction sites such as $\pi - \pi$ stacking of aromatic side chains and hydrogen bond motifs -NH3+····-OOC- formed during the self-assembly process. Furthermore, we have used ToF-SIMS to assess damage at molecular length scales, showing that this kind of surface characterization technique can be used to assess low molecular weight synthons following LCTEM

analysis. This showed that the morphology of the assembled structure may remain intact, but over time, molecular level damage is inevitable. Together, we have found that the elongation kinetics of FF in LCTEM are consistent with the unidirectional elongation observed by bulk microfluidic conditions. Further, nucleation and early stage assembly kinetics of FF were slower in LCTEM compared to bulk experiments, which allowed us to capture the early stage assembly of FF and notably a linear growth trend in FF nanotube diameter, a mechanism not previously observed. More generally, this study demonstrates LCTEM can be a useful tool for studying the self-assembly and dynamics of wide range of soft materials and biological systems such as organic small molecules, amyloid fiber formation and inhibition, and cellular machinery like actin filaments and microtubules.

METHODS

Diphenylalanine (FF) Assembly. Stock solutions of diphenylalanine (Sigma-Aldrich) were prepared by vortexing 2 mg mL⁻¹ FF for 2 min in an appropriate solvent. Self-assembly in water was initiated by heating the dispersed solution to 80 °C for 1 h and allowed to cool to room temperature. Self-assembly in alcohols was initiated immediately after vortexing, and the dispersed solution was left unaltered at room temperature. For transmission electron microscopy, aliquots of FF dispersed in water were taken after 30 min of cooling at room temperature. For liquid-cell transmission electron microscopy, vortexed stock solutions were drop-casted onto the liquid-cell chips, and assembly was initiated *in situ*.

Transmission Electron Microscopy (TEM). TEM and LCTEM of bulk and *in situ* synthesized FF were performed using a JEOL JEM-ARM300F GrandARM TEM (Tokyo, Japan) with a Gatan OneView-IS camera (Pleasanton, CA, USA) and K3-IS camera (Pleasanton, CA, USA) operated at 300 keV. Time lapse LCTEM data were acquired using Camtasia Studio 2018 (TechSmith Corporation, Okemos, MI, USA). For *post-mortem* analysis, LCTEM chips were opened carefully and washed gently with distilled water. Bottom chips were then placed on the standard single-tilt TEM holder, and images were collected in BF-TEM mode.

Liquid-Cell Transmission Electron Microscopy (LCTEM). A Protochips Poseidon Select Heating holder (Morrisville, NC, USA) was used to collect LCTEM data. Milli-Q water was used to prefill the lines of the holder in all LCTEM experiments. LCTEM chips with 50 nm-thick, $200 \, \mu \text{m} \times 50 \, \mu \text{m}$ window SiN_x membranes were cleaned in acetone followed by methanol, dried, and subsequently glow discharged in a PELCO easiGlow glow discharge unit for 5 min. Next, 0.2 µL of FF dispersed in solvent was pipetted manually onto the bottom chip, and then, the liquid-cell was assembled with the windows (50 μ m × 200 μ m) aligned perpendicularly (50 μ m × 50 μ m LCTEM viewing area) and the lines of the holder were sealed off without external flow. Following a leak check, a liquid-cell holder was inserted into the column of the microscope, and the cell was heated to 80 °C for 1 h using a Protochips temperature controller at a rate of 1 °C s⁻¹, followed by the cell being allowed to cool to room temperature for 30 min. During heating and cooling cycles, the liquidcell was not exposed to the electron beam. Images and movies were recorded in BF-TEM mode. In some experiments, liquid thickness was manipulated by carefully pulling out the excess water through the flow channels. Pulse image acquisitions were automated using the SerialEM scripting interface. All TEM alignments, beam settings, dose settings, and calibrations were conducted prior to the liquid-cell experiments using standard gold nanoparticles or diffraction grating waffle TEM sample.

LCTEM Electron Flux Measurements. Beam current (pA cm⁻²), measured using the small screen in the microscope, was calibrated using a Faraday cup (nA). Calibration data were obtained for various electron beam parameters, like spot size, condenser aperture, and emission current, in the linear regime over the range of beam currents used for LCTEM experiments. At the start of each experiment, the

calibrated beam current from the small screen was measured for appropriate spot size, condenser lens system, and emission current used for that specific experiment. The beam diameter (\mathring{A}^2) was measured for the appropriate magnification. This was used along with calibrated beam current (nA) to calculate electron flux (e $^ \mathring{A}^{-2}$ s $^{-1}$). These measurements were conducted before the LCTEM experiments using a single tilt holder or blank LCTEM chips without a liquid sample. The settings were left unaltered for subsequent LCTEM experiments.

X-ray Scattering Analysis. Small-angle X-ray scattering (SAXS) experiments were conducted at the 5-ID-D beamline of the Dupont-Northwestern-Dow Collaborative Access Team (DND-CAT) at the Advanced Photon Source, Argonne National Laboratory. Samples of 2 mg mL⁻¹ FF in water were prepared and loaded into 1.5 mm quartz capillaries for variable temperature SAXS. The capillaries were then sealed with epoxy to prevent solvent evaporation prior to data acquisition. Capillaries were loaded into a variable temperature multicapillary holder. The samples were heated to 80 °C and held for 1 h to disperse any preformed aggregates before acquiring a scattering pattern at 80 °C. Samples were then cooled to 30 °C at a rate of 2 °C min⁻¹. After reaching the temperature set point, patterns were obtained every 2 min for 60 min. Samples were then heated back to 80 °C at 2 °C min⁻¹. After reaching the set point, patterns were acquired after 1 h. Two-dimensional scattering patterns were obtained from 10 s exposure using a Rayonix MX170-HS CCD area detector using a 0.5 s exposure time to X-rays with a wavelength of $\lambda = 0.7293$ Å and a sample-to-detector distance of 8.5 m. The 2D data were azimuthally averaged to yield 1D scattering patterns as intensity versus q. Incoherent background scattering was measured by acquiring scattering patterns for a water-loaded capillary in the absence of FF. The experimental data was fit to a power law of the form $I(q) = A + Bq^{-m} + Cq^2$ and subtracted from the FF data, where 2 $\leq m \leq 4$. For the room temperature X-ray scattering patterns, 2 mg mL⁻¹ FF monomers were dispersed in water and heated to 80 °C and then cooled ambiently to room temperature overnight, resulting in the formation of visible powdery precipitates. The powders were then removed from the vials, mounted on Kapton tape adhered to a plastic washer, and dried for several days. Simultaneous SAXS, MAXS, and WAXS patterns were then obtained for the powders at the 5-ID-D beamline, and data analysis followed the same procedure as that for the variable temperature solution SAXS data.

ToF-SIMS Analysis. TOF-SIMS measurements were performed using a Physical Electronics Inc. (PHI, Chanhassen, MN, USA) TRIFT III mass spectrometer equipped with a gallium ion primary beam source. Measurements were performed with a raster size of 100 μ m, a voltage of 25 kV, and analytical charge compensation. Mosaic mapping on a 0.5 mm \times 0.5 mm area surrounding the irradiated window was performed on both (top and bottom) liquid-cell chips to yield a secondary ion map of the SiN $_x$ surface from 0 to 1850 m/z.

ASSOCIATED CONTENT

Supporting Information

The Supporting Information is available free of charge at https://pubs.acs.org/doi/10.1021/acsnano.1c06130.

Figures of schematics of LCTEM chips, LCTEM snapshots, FF growth measurements, TEM images, line profiles, *in situ* SAXS, MAXS, and WAXS patterns, ToF-SIMS maps, ToF-SIMS spectra and discussions of *post-mortem* analysis, heating of preformed FF within the liquid-cell, and X-ray scattering of FF assemblies (PDF)

Movie of LCTEM of in situ growth of FF nanotubes (AVI)

Movie of LCTEM of early stage assembly of FF monomers (AVI)

Movie of LCTEM of preformed FF assemblies within the liquid-cell (AVI) $\,$

Movie of LCTEM of preformed FF assemblies within the liquid-cell (AVI)

AUTHOR INFORMATION

Corresponding Author

Nathan C. Gianneschi — Department of Chemistry,
International Institute for Nanotechnology, Simpson Querrey
Institute, Chemistry of Life Processes Institute, Northwestern
University, Evanston, Illinois 60208, United States;
Department of Materials Science & Engineering, Department
of Biomedical Engineering, Department of Pharmacology,
Northwestern University, Evanston, Illinois 60208, United
States; Orcid.org/0000-0001-9945-5475;
Email: nathan.gianneschi@northwestern.edu

Authors

Karthikeyan Gnanasekaran — Department of Chemistry, International Institute for Nanotechnology, Simpson Querrey Institute, Chemistry of Life Processes Institute, Northwestern University, Evanston, Illinois 60208, United States; Department of Materials Science & Engineering, Department of Biomedical Engineering, Department of Pharmacology, Northwestern University, Evanston, Illinois 60208, United States; orcid.org/0000-0001-6635-0888

Joanna Korpanty — Department of Chemistry, International Institute for Nanotechnology, Simpson Querrey Institute, Chemistry of Life Processes Institute, Northwestern University, Evanston, Illinois 60208, United States; orcid.org/0000-0002-9274-5936

Or Berger — Department of Chemistry, International Institute for Nanotechnology, Simpson Querrey Institute, Chemistry of Life Processes Institute, Northwestern University, Evanston, Illinois 60208, United States; Department of Materials Science & Engineering, Department of Biomedical Engineering, Department of Pharmacology, Northwestern University, Evanston, Illinois 60208, United States

Nicholas Hampu — Department of Chemistry, International Institute for Nanotechnology, Simpson Querrey Institute, Chemistry of Life Processes Institute, Northwestern University, Evanston, Illinois 60208, United States; Department of Materials Science & Engineering, Department of Biomedical Engineering, Department of Pharmacology, Northwestern University, Evanston, Illinois 60208, United States; orcid.org/0000-0002-8127-1034

Michal Halperin-Sternfeld — Department of Oral Biology, The Goldschleger School of Dental Medicine, Sackler Faculty of Medicine, Tel Aviv University, Tel Aviv 6997801, Israel; The Center for Nanoscience and Nanotechnology, Tel Aviv University, Tel Aviv 6997801, Israel; orcid.org/0000-0001-9242-0616

Dana Cohen-Gerassi — Department of Oral Biology, The Goldschleger School of Dental Medicine, Sackler Faculty of Medicine, Tel Aviv University, Tel Aviv 6997801, Israel; The Center for Nanoscience and Nanotechnology and Department of Materials Science and Engineering, Iby and Aladar Fleischman Faculty of Engineering, Tel Aviv University, Tel Aviv 6997801, Israel; orcid.org/0000-0002-4172-8511

Lihi Adler-Abramovich — Department of Oral Biology, The Goldschleger School of Dental Medicine, Sackler Faculty of Medicine, Tel Aviv University, Tel Aviv 6997801, Israel; The Center for Nanoscience and Nanotechnology, Tel Aviv University, Tel Aviv 6997801, Israel; orcid.org/0000-0003-3433-0625

Complete contact information is available at: https://pubs.acs.org/10.1021/acsnano.1c06130

Author Contributions

*K.G. and J.K. contributed equally to this work.

Notes

The authors declare no competing financial interest.

ACKNOWLEDGMENTS

This research used the EPIC facility of Northwestern University's NUANCE Center, which has received support from the Soft and Hybrid Nanotechnology Experimental (SHyNE) Resource (NSF ECCS-1542205); the MRSEC program (NSF DMR-1720139) at the Materials Research Center; the International Institute for Nanotechnology (IIN); the Keck Foundation; and the State of Illinois, through the IIN. Research reported in this publication was supported in part by instrumentation provided by the Office of The Director, National Institutes of Health of the National Institutes of Health under Award Number S10OD026871. The content is solely the responsibility of the authors and does not necessarily represent the official views of the National Institutes of Health. Furthermore, the authors would like to thank the Army Research Office (W911NF-17-1-0326, W911NF-18-1-0359, MURI W911NF-15-1-0568) and the National Science Foundation (CHE-MSN 1905270) for support. K.G. is appreciative of a postdoctoral fellowship from the Human Frontier Science Program (LT000869/2018-C). J.K. gratefully acknowledges support from the Ryan Fellowship and the International Institute for Nanotechnology at Northwestern University. The authors acknowledge a Clore scholarship (M.H.-S), BSF (grant No. 2018102) (M.H.-S), GRTF travel grant (M.H.-S), and the Israel Science Foundation (grant No. 1732/17) (L.A.-A.) for support. Portions of this work were performed at the DuPont-Northwestern-Dow Collaborative Access Team (DND-CAT) located at Sector 5 of the Advanced Photon Source (APS). DND-CAT is supported by Northwestern University, E.I. DuPont de Nemours & Co., and The Dow Chemical Company. This research used resources of the APS, a U.S. Department of Energy (DOE) Office of Science User Facility operated for the DOE Office of Science by Argonne National Laboratory under Contract No. DE-AC02-06CH11357. Data were collected using an instrument funded by the NSF under Award Number 0960140. The authors would like to acknowledge the Gianneschi and Adler-Abramovich research groups for fruitful discussions.

REFERENCES

- (1) Gorbitz, C. H. Nanotube Formation by Hydrophobic Dipeptides. *Chem. Eur. J.* **2001**, *7*, 5153–5159.
- (2) Görbitz, C. H. The Structure of Nanotubes Formed by Diphenylalanine, the Core Recognition Motif of Alzheimer's Beta-Amyloid Polypeptide. *Chem. Commun.* **2006**, 2332–2334.
- (3) Rambaran, R. N.; Serpell, L. C. Amyloid Fibrils: Abnormal Protein Assembly. *Prion* **2008**, *2*, 112–117.
- (4) Reches, M.; Gazit, E. Casting Metal Nanowires within Discrete Self-Assembled Peptide Nanotubes. *Science* **2003**, *300*, 625–627.
- (5) Yan, X.; Zhu, P.; Li, J. Self-Assembly and Application of Diphenylalanine-Based Nanostructures. *Chem. Soc. Rev.* **2010**, 39, 1877–1890
- (6) Sun, B.; Riegler, H.; Dai, L.; Eickelmann, S.; Li, Y.; Li, G.; Yang, Y.; Li, Q.; Fu, M.; Fei, J.; Li, J. Directed Self-Assembly of Dipeptide Single Crystal in a Capillary. ACS Nano 2018, 12, 1934–1939.

- (7) Li, Q.; Jia, Y.; Dai, L.; Yang, Y.; Li, J. Controlled Rod Nanostructured Assembly of Diphenylalanine and Their Optical Waveguide Properties. ACS Nano 2015, 9, 2689–2695.
- (8) Adler-Abramovich, L.; Reches, M.; Sedman, V. L.; Allen, S.; Tendler, S. J.; Gazit, E. Thermal and Chemical Stability of Diphenylalanine Peptide Nanotubes: Implications for Nanotechnological Applications. *Langmuir* **2006**, *22*, 1313–1320.
- (9) Hill, R. J. A.; Sedman, V. L.; Allen, S.; Williams, P.; Paoli, M.; Adler-Abramovich, L.; Gazit, E.; Eaves, L.; Tendler, S. J. B. Alignment of Aromatic Peptide Tubes in Strong Magnetic Fields. *Adv. Mater.* **2007**, *19*, 4474–4479.
- (10) Adler-Abramovich, L.; Gazit, E. The Physical Properties of Supramolecular Peptide Assemblies: From Building Block Association to Technological Applications. *Chem. Soc. Rev.* **2014**, *43*, 6881–6893.
- (11) Song, Y.; Challa, S. R.; Medforth, C. J.; Qiu, Y.; Watt, R. K.; Pena, D.; Miller, J. E.; Swol, F. v.; Shelnutt, J. A. Synthesis of Peptide-Nanotube Platinum-Nanoparticle Composites. *Chem. Commun.* **2004**, 1044–1045.
- (12) Yan, X.; Cui, Y.; He, Q.; Wang, K.; Li, J.; Mu, W.; Wang, B.; Ou-Yang, Z. C. Reversible Transitions between Peptide Nanotubes and Vesicle-Like Structures Including Theoretical Modeling Studies. *Chem. Eur. J.* **2008**, *14*, 5974–5980.
- (13) Mason, T. O.; Chirgadze, D. Y.; Levin, A.; Adler-Abramovich, L.; Gazit, E.; Knowles, T. P.; Buell, A. K. Expanding the Solvent Chemical Space for Self-Assembly of Dipeptide Nanostructures. *ACS Nano* **2014**, *8*, 1243–1253.
- (14) Williamson, M. J.; Tromp, R. M.; Vereecken, P. M.; Hull, R.; Ross, F. M. Dynamic Microscopy of Nanoscale Cluster Growth at the Solid-Liquid Interface. *Nat. Mater.* **2003**, *2*, 532–536.
- (15) Ross, F. M. Opportunities and Challenges in Liquid Cell Electron Microscopy. *Science* **2015**, *350*, aaa9886.
- (16) Smith, B. J.; Parent, L. R.; Overholts, A. C.; Beaucage, P. A.; Bisbey, R. P.; Chavez, A. D.; Hwang, N.; Park, C.; Evans, A. M.; Gianneschi, N. C.; Dichtel, W. R. Colloidal Covalent Organic Frameworks. *ACS Cent. Sci.* **2017**, *3*, 58–65.
- (17) Zheng, H.; Smith, R. K.; Jun, Y. W.; Kisielowski, C.; Dahmen, U.; Alivisatos, A. P. Observation of Single Colloidal Platinum Nanocrystal Growth Trajectories. *Science* **2009**, 324, 1309–1312.
- (18) Yuk, J. M.; Park, J.; Ercius, P.; Kim, K.; Hellebusch, D. J.; Crommie, M. F.; Lee, J. Y.; Zettl, A.; Alivisatos, A. P. High-Resolution EM of Colloidal Nanocrystal Growth Using Graphene Liquid Cells. *Science* **2012**, *336*, 61–64.
- (19) Woehl, T. J.; Evans, J. E.; Arslan, I.; Ristenpart, W. D.; Browning, N. D. Direct *in Situ* Determination of the Mechanisms Controlling Nanoparticle Nucleation and Growth. *ACS Nano* **2012**, *6*, 8599–8610.
- (20) Verch, A.; Pfaff, M.; De Jonge, N. Exceptionally Slow Movement of Gold Nanoparticles at a Solid/Liquid Interface Investigated by Scanning Transmission Electron Microscopy. *Langmuir* **2015**, *31*, 6956–6964.
- (21) Ahmad, N.; Wang, G.; Nelayah, J.; Ricolleau, C.; Alloyeau, D. Exploring the Formation of Symmetric Gold Nanostars by Liquid-Cell Transmission Electron Microscopy. *Nano Lett.* **2017**, *17*, 4194–4201.
- (22) Ianiro, A.; Wu, H.; Van Rijt, M. M. J.; Vena, M. P.; Keizer, A. D. A.; Esteves, A. C. C.; Tuinier, R.; Friedrich, H.; Sommerdijk, N.; Patterson, J. P. Liquid-Liquid Phase Separation during Amphiphilic Self-Assembly. *Nat. Chem.* **2019**, *11*, 320–328.
- (23) Parent, L. R.; Bakalis, E.; Ramirez-Hernandez, A.; Kammeyer, J. K.; Park, C.; De Pablo, J.; Zerbetto, F.; Patterson, J. P.; Gianneschi, N. C. Directly Observing Micelle Fusion and Growth in Solution by Liquid-Cell Transmission Electron Microscopy. *J. Am. Chem. Soc.* **2017**, *139*, 17140–17151.
- (24) Early, J. T.; Yager, K. G.; Lodge, T. P. Direct Observation of Micelle Fragmentation *via in Situ* Liquid-Phase Transmission Electron Microscopy. *ACS Macro Lett.* **2020**, *9*, 756–761.
- (25) Patterson, J. P.; Abellan, P.; Denny, M. S., Jr.; Park, C.; Browning, N. D.; Cohen, S. M.; Evans, J. E.; Gianneschi, N. C. Observing the Growth of Metal-Organic Frameworks by *in Situ*

- Liquid-Cell Transmission Electron Microscopy. J. Am. Chem. Soc. 2015, 137, 7322-7328.
- (26) Vailonis, K. M.; Gnanasekaran, K.; Powers, X. B.; Gianneschi, N. C.; Jenkins, D. M. Elucidating the Growth of Metal-Organic Nanotubes Combining Isoreticular Synthesis with Liquid-Cell Transmission Electron Microscopy. *J. Am. Chem. Soc.* **2019**, *141*, 10177–10182.
- (27) Wang, W.; Yan, H.; Anand, U.; Mirsaidov, U. Visualizing the Conversion of Metal-Organic Framework Nanoparticles into Hollow Layered Double Hydroxide Nanocages. *J. Am. Chem. Soc.* **2021**, *143*, 1854–1862.
- (28) Cookman, J.; Hamilton, V.; Price, L. S.; Hall, S. R.; Bangert, U. Visualising Early-Stage Liquid Phase Organic Crystal Growth *via* Liquid Cell Electron Microscopy. *Nanoscale* **2020**, *12*, 4636–4644.
- (29) Park, J.; Park, H.; Ercius, P.; Pegoraro, A. F.; Xu, C.; Kim, J. W.; Han, S. H.; Weitz, D. A. Direct Observation of Wet Biological Samples by Graphene Liquid-Cell Transmission Electron Microscopy. *Nano Lett.* **2015**, *15*, 4737–4744.
- (30) Peckys, D. B.; De Jonge, N. Liquid Scanning Transmission Electron Microscopy: Imaging Protein Complexes in Their Native Environment in Whole Eukaryotic Cells. *Microsc. Microanal.* **2014**, *20*, 346–365.
- (31) Wu, H.; Friedrich, H.; Patterson, J. P.; Sommerdijk, N. A. J. M.; Jonge, N. Liquid-Phase Electron Microscopy for Soft Matter Science and Biology. *Adv. Mater.* **2020**, *32*, 2001582.
- (32) Parent, L. R.; Gnanasekaran, K.; Korpanty, J.; Gianneschi, N. C. 100th Anniversary of Macromolecular Science Viewpoint: Polymeric Materials by *in Situ* Liquid-Phase Transmission Electron Microscopy. *ACS Macro Lett.* **2021**, *10*, 14–38.
- (33) He, K.; Shokuhfar, T.; Shahbazian-Yassar, R. Imaging of Soft Materials Using *in Situ* Liquid-Cell Transmission Electron Microscopy. *J. Phys.: Condens. Matter* **2019**, *31*, 103001.
- (34) Woehl, T. J.; Abellan, P. Defining the Radiation Chemistry during Liquid-Cell Electron Microscopy to Enable Visualization of Nanomaterial Growth and Degradation Dynamics. *J. Microsc.* **2017**, 265, 135–147.
- (35) Korpanty, J.; Parent, L. R.; Gianneschi, N. C. Enhancing and Mitigating Radiolytic Damage to Soft Matter in Aqueous Phase Liquid-Cell Transmission Electron Microscopy in the Presence of Gold Nanoparticle Sensitizers or Isopropanol Scavengers. *Nano Lett.* **2021**, 21, 1141–1149.
- (36) Von Sonntag, C. Free-Radical-Induced Chain Scission and Cross-Linking of Polymers in Aqueous Solution—An Overview. *Radiat. Phys. Chem.* **2003**, *67*, 353—359.
- (37) Schneider, N. M.; Norton, M. M.; Mendel, B. J.; Grogan, J. M.; Ross, F. M.; Bau, H. H. Electron—Water Interactions and Implications for Liquid Cell Electron Microscopy. *J. Phys. Chem. C* **2014**, *118*, 22373—22382.
- (38) Grogan, J. M.; Schneider, N. M.; Ross, F. M.; Bau, H. H. Bubble and Pattern Formation in Liquid Induced by an Electron Beam. *Nano Lett.* **2014**, *14*, 359–364.
- (39) Wang, M.; Leff, A. C.; Li, Y.; Woehl, T. J. Visualizing Ligand-Mediated Bimetallic Nanocrystal Formation Pathways with *in Situ* Liquid-Phase Transmission Electron Microscopy Synthesis. *ACS Nano* 2021, 15, 2578–2588.
- (40) Touve, M. A.; Carlini, A. S.; Gianneschi, N. C. Self-Assembling Peptides Imaged by Correlated Liquid-Cell Transmission Electron Microscopy and MALDI-Imaging Mass Spectrometry. *Nat. Commun.* **2019**, *10*, 4837.
- (41) Vandenbussche, E. J.; Flannigan, D. J. Reducing Radiation Damage in Soft Matter with Femtosecond-Timed Single-Electron Packets. *Nano Lett.* **2019**, *19*, 6687–6694.
- (42) Arnon, Z. A.; Vitalis, A.; Levin, A.; Michaels, T. C. T.; Caflisch, A.; Knowles, T. P. J.; Adler-Abramovich, L.; Gazit, E. Dynamic Microfluidic Control of Supramolecular Peptide Self-Assembly. *Nat. Commun.* **2016**, *7*, 13190.
- (43) Brahmachari, S.; Arnon, Z. A.; Frydman-Marom, A.; Gazit, E.; Adler-Abramovich, L. Diphenylalanine as a Reductionist Model for

- the Mechanistic Characterization of Beta-Amyloid Modulators. ACS Nano 2017, 11, 5960-5969.
- (44) Frederix, P. W.; Ulijn, R. V.; Hunt, N. T.; Tuttle, T. Virtual Screening for Dipeptide Aggregation: Toward Predictive Tools for Peptide Self-Assembly. *J. Phys. Chem. Lett.* **2011**, *2*, 2380–2384.
- (45) Guo, C.; Luo, Y.; Zhou, R.; Wei, G. Probing the Self-Assembly Mechanism of Diphenylalanine-Based Peptide Nanovesicles and Nanotubes. *ACS Nano* **2012**, *6*, 3907–3918.
- (46) Xiong, Q.; Jiang, Y.; Cai, X.; Yang, F.; Li, Z.; Han, W. Conformation Dependence of Diphenylalanine Self-Assembly Structures and Dynamics: Insights from Hybrid-Resolution Simulations. *ACS Nano* **2019**, *13*, 4455–4468.
- (47) Jeon, J.; Mills, C. E.; Shell, M. S. Molecular Insights into Diphenylalanine Nanotube Assembly: All-Atom Simulations of Oligomerization. *J. Phys. Chem. B* **2013**, *117*, 3935–3943.
- (48) Keskin, S.; Kunnas, P.; De Jonge, N. Liquid-Phase Electron Microscopy with Controllable Liquid Thickness. *Nano Lett.* **2019**, *19*, 4608–4613.
- (49) Kröger, R.; Verch, A. Liquid Cell Transmission Electron Microscopy and the Impact of Confinement on the Precipitation from Supersaturated Solutions. *Minerals* **2018**, *8*, 21.
- (50) Wang, M.; Dissanayake, T. U.; Park, C.; Gaskell, K.; Woehl, T. J. Nanoscale Mapping of Nonuniform Heterogeneous Nucleation Kinetics Mediated by Surface Chemistry. *J. Am. Chem. Soc.* **2019**, *141*, 13516–13524.
- (51) Kim, J.; Han, T. H.; Kim, Y. I.; Park, J. S.; Choi, J.; Churchill, D. G.; Kim, S. O.; Ihee, H. Role of Water in Directing Diphenylalanine Assembly into Nanotubes and Nanowires. *Adv. Mater.* **2010**, 22, 583–587
- (52) Wang, Y.; Peng, X. X.; Abelson, A.; Zhang, B. K.; Qian, C.; Ercius, P.; Wang, L. W.; Law, M.; Zheng, H. M. *In Situ* TEM Observation of Neck Formation during Oriented Attachment of PbSe Nanocrystals. *Nano Res.* **2019**, *12*, 2549–2553.
- (53) Nielsen, M. H.; Li, D.; Zhang, H.; Aloni, S.; Han, T. Y.; Frandsen, C.; Seto, J.; Banfield, J. F.; Colfen, H.; De Yoreo, J. J. Investigating Processes of Nanocrystal Formation and Transformation *via* Liquid Cell TEM. *Microsc. Microanal.* **2014**, *20*, 425–436.
- (54) Liao, H. G.; Cui, L.; Whitelam, S.; Zheng, H. Real-Time Imaging of Pt3Fe Nanorod Growth in Solution. *Science* **2012**, 336, 1011–1014.
- (55) Zhang, N.; Geronimo, I.; Paneth, P.; Schindelka, J.; Schaefer, T.; Herrmann, H.; Vogt, C.; Richnow, H. H. Analyzing Sites of OH Radical Attack (Ring vs. Side Chain) in Oxidation of Substituted Benzenes via Dual Stable Isotope Analysis (δ^{13} C and δ^{2} H). Sci. Total Environ. 2016, 542, 484–494.
- (56) Hayon, E.; Ibata, T.; Lichtin, N. N.; Simic, M. Sites of Attack of Hydroxyl Radicals on Amides in Aqueous Solution. *J. Am. Chem. Soc.* **1970**, *92*, 3898–3903.
- (57) Hambly, D. M.; Gross, M. L. Microsecond Time-Scale Hydroxyl Radical Profiling of Solvent-Accessible Protein Residues. In *Comprehensive Analytical Chemistry: Protein Mass Spectrometry*; Whitelegge, J. P., Ed.; Elsevier: Amsterdam, 2008; pp 151–177.
- (58) Da Silva, G. Oxidation of Carboxylic Acids Regenerates Hydroxyl Radicals in the Unpolluted and Nighttime Troposphere. *J. Phys. Chem. A* **2010**, *114*, 6861–6869.
- (59) Talian, I.; Orinak, A.; Preisler, J.; Heile, A.; Onofrejova, L.; Kaniansky, D.; Arlinghaus, H. F. Comparative TOF-SIMS And MALDI TOF-MS Analysis on Different Chromatographic Planar Substrates. *J. Sep. Sci.* **2007**, *30*, 2570–2582.
- (60) Chakraborty, P.; Tang, Y.; Guterman, T.; Arnon, Z. A.; Yao, Y.; Wei, G.; Gazit, E. Co-Assembly between Fmoc Diphenylalanine and Diphenylalanine within a 3D Fibrous Viscous Network Confers Atypical Curvature and Branching. *Angew. Chem., Int. Ed.* **2020**, *59*, 23731–23739.
- (61) Reimer, L.; Kohl, H. Transmission Electron Microscopy: Physics of Image Formation; Springer: New York, 2008; pp 141–194.
- (62) Patterson, J. P.; Abellan, P.; Denny, M. S.; Park, C.; Browning, N. D.; Cohen, S. M.; Evans, J. E.; Gianneschi, N. C. Observing the

Self-Assembly of Metal-Organic Frameworks by in Situ Liquid-Cell TEM. Microsc. Microanal. 2015, 21, 2445–2446.